Thermodynamic phase profiles of optically thin midlatitude clouds and their relation to temperature

C. M. Naud, A. D. del Genio, M. Haeffelin, Y. Morille, V. Noel, J. -C. Dupont, D. D. Turner, C. Lo, J. Comstock

JOURNAL OF GEOPHYSICAL RESEARCH, VOL. 115, D11202, doi:10.1029/2009JD012889, 2010

Thermodynamic phase profiles of optically thin midlatitude clouds and their relation to temperature

C. M. Naud,[1] A. D. Del Genio,[2] M. Haeffelin,[3] Y. Morille,[3] V. Noel,[3] J.-C. Dupont,[3] D. D. Turner,[4] C. Lo,[5] and J. Comstock[5]

Received 24 July 2009; revised 11 January 2010; accepted 19 January 2010; published 3 June 2010.

[1] The relationship between cloud thermodynamic phase and temperature in some aircraft measurements conducted in midlatitude frontal clouds suggests that significant liquid does not exist at temperatures colder than 258 K. This data set is often used to verify parameterizations of cloud phase in general circulation models. However, other aircraft campaigns and different instruments suggest a different relationship. Here we examine the temperature-phase relationship for midlatitude optically thin winter clouds. Cloud phase and temperature profiles derived from 5 years of ground-based lidar depolarization and radiosonde measurements are analyzed for two midlatitude locations: the U. S. Atmospheric Radiation Measurement Program Southern Great Plains site and the Site Instrumental de Recherche par Télédétection Atmosphérique in France. Because lidars are attenuated in optically thick clouds, the data set only includes clouds with optical thickness of <3. Cloud phase is obtained by using the classical method based on a depolarization ratio threshold of 11% for differentiating liquid from ice. The frequency of occurrence of clouds either completely liquid or completely glaciated in the temperature range from 233 to 273 K is similar to previous observations in the midlatitudes but somewhat greater than in the Arctic. The relationship between ice phase occurrence and temperature only slightly changes between cloud base and top. At both sites, liquid is more prevalent at colder temperatures than has been found previously in some thicker frontal clouds, suggesting different processes for glaciation in nonfrontal optically thin clouds.

Citation: Naud, C. M., A. D. Del Genio, M. Haeffelin, Y. Morille, V. Noel, J.-C. Dupont, D. D. Turner, C. Lo, and J. Comstock (2010), Thermodynamic phase profiles of optically thin midlatitude clouds and their relation to temperature, *J. Geophys. Res.*, *115*, D11202, doi:10.1029/2009JD012889.

1. Introduction

[2] To more accurately predict cloud feedbacks in a warming climate, general circulation models (GCMs) need to improve their parameterizations of cloud microphysical processes. Midlevel altostratus and altocumulus clouds receive less attention than other cloud types but are of particular interest, as they occur in a temperature range where cloud phase can either be liquid, ice, or mixed. Assumptions that control the relative amounts of liquid and ice in clouds can have a significant impact on cloud feedbacks in a changing climate [*Mitchell et al.*, 1989; *Li and Le Treut*, 1992]. However, whether cloud phase partitioning in a GCM is directly dictated by observations [*Del Genio et al.*, 1996] or the result of a more complex prognostic microphysics scheme [*Wilson and Ballard*, 1999; *Rotstayn et al.*, 2000; *Morrison and Gettelman*, 2008], models have to rely heavily on measurements for either parameterization design and evaluation.

[3] Initially, cloud phase measurements came from aircraft campaigns, but conflicting results were found: *Feigelson* [1978] found supercooled liquid clouds at temperatures as cold as −40°C over the continental ex-USSR, whereas *Bower et al.* [1996] did not find significant amounts of liquid in clouds colder than −15°C for locations around the British Isles. These disagreements have led to different parameterization choices that influence the temperature dependence of cloud phase in GCMs [*Del Genio et al.*, 1996; *Rotstayn et al.*, 2000; *Lopez*, 2002]. These results hinted that the data set in *Bower et al.* [1996] may have undersampled nonfrontal clouds relative to the *Feigelson* [1978] data sets, as discussed by *Rotstayn et al.* [2000]. Indeed, the cloud thermodynamic phase can be influenced

[1]Department of Applied Physics and Applied Mathematics, Columbia University and Goddard Institute for Space Studies, New York, New York, USA.
[2]NASA Goddard Institute for Space Studies, New York, New York, USA.
[3]Laboratoire de Météorologie Dynamique and Institut Pierre Simon Laplace, Palaiseau, France.
[4]Space Science and Engineering Center, University of Wisconsin–Madison, Madison, Wisconsin, USA.
[5]Pacific Northwest National Laboratory, Richland, Washington, USA.

0148-0227/10/2009JD012889

by factors other than temperature, e.g., the dynamics, the age of the clouds, or the concentration of ice nuclei [*Fridlind et al.*, 2007].

[4] *Naud et al.* [2006] used satellite visible and infrared retrievals of cloud thermodynamic phase and temperature and reanalysis meteorological fields to study the impact of atmospheric dynamics on cloud phase in the northern Atlantic and Pacific midlatitude storm tracks. They found that liquid does not normally persist for temperatures much below −15°C in the frontal regions of rising motion greater than 10 hPa h^{-1} in midlatitude cyclones, but it does persist to a somewhat greater extent in the frontal region of the more vigorous west Atlantic midlatitude cyclones and to much colder temperatures in the extensive subsidence region behind the cold front. Persistence of liquid at cold temperatures was also observed globally by *Giraud et al.* [2001], who analyzed satellite passive polarization measurements of cloud top phase and their relationship to temperature over ocean and land. Similarly, *Hogan et al.* [2004] observed supercooled liquid cloud layers in midlatitude regions at temperatures much colder than −15°C and not necessarily confined to cloud top using ground-based and spacecraft data.

[5] Here we investigate the limitations of a unique relationship between cloud phase and temperature by looking at a different type of cloud than those sampled by *Bower et al.* [1996]: optically thin winter clouds that typically occur in fair weather situations, in advance of fronts or in the subsidence zone of midlatitude cyclones. Furthermore, we extend work previously done with passive satellite observations by observing different levels of the same cloud. Passive space-based observations can only sample near cloud top where glaciation may not occur at the same rate as at lower levels within the cloud (although low cloud optical thicknesses can cause the observations to be more representative of lower levels in the cloud or the entire cloud). For example, Arctic clouds often exhibit a layer of supercooled droplets at the top of a cloud otherwise composed mainly of ice [*Intrieri et al.*, 2002; *Shupe et al.*, 2006; *McFarquhar et al.*, 2007], and this has also been observed in midlatitude mixed phase clouds [*Rauber and Tokay*, 1991; *Heymsfield et al.*, 1991; *Fleishauer et al.*, 2002; *Hogan et al.*, 2003a; *Carey et al.*, 2008]. Consequently, to verify whether supercooled liquid is restricted to cloud top when temperatures are well below −15°C in nonfrontal regions, a long-term data set that can sample all cloud levels for their phase is needed.

[6] Active instruments such as lidars can penetrate the interior of clouds and thus provide coincident information on phase at all levels and often at high vertical resolution. Because lidar beams are attenuated in dense clouds, only optically thin clouds with visible optical depth of less than 3 can be fully observed. Cloud phase can be obtained if the lidar possesses a channel with depolarization capability [*Sassen*, 1991]. It is still possible to get some information on the cloud phase from lidar data if depolarization is missing [*Hogan et al.*, 2003a, 2003b, 2004], but this is limited to detecting highly reflective liquid layers in clouds and thus cannot give a full profile of ice phase occurrence. In this paper, we use long-term ground-based lidar depolarization profiles to derive thermodynamic phase profiles and explore the presence of liquid at cold temperature at all levels from cloud base to top, specifically for optically thin clouds.

[7] We use data from two locations situated on either side of the north Atlantic: the Site Instrumental de Recherche par Télédétection Atmosphérique (SIRTA; 48.7°N–2.2°E) of the Institut Pierre Simon Laplace, based south of Paris, France [*Haeffelin et al.*, 2005] and the U. S. Department of Energy Atmospheric Radiation Measurement Program (ARM) [*Ackerman and Stokes*, 2003] Southern Great Plains site in Oklahoma (SGP; 36.6°N–97.5°W). For both locations, we selected lidar data for winter months (November–March): 2002–2007 for SIRTA and 1998–2003 for SGP. Summer months were excluded because environmental conditions are very different between summer (more convective) and winter months at SGP, while the synoptic situation at SIRTA exhibits less contrast from one season to another. Thus, environmental conditions and synoptic activity are more similar in wintertime between the SGP and SIRTA sites than in other seasons. This similarity is important to limit the impact of factors other than temperature on cloud phase. Also, in order to accurately calibrate the depolarization ratios, a significant portion of the lidar profiles should be dominated by pure molecular signal and thus lacking clouds and aerosols. Aerosols in winter at SGP are largely confined to the lowest kilometer above the lidar and are less of a problem then [*Turner et al.*, 2001]. Consequently, all our conclusions are only valid for optically thin clouds that occur preferentially during winter months. However, this still constitutes an important subset of nonfrontal clouds, with half of the winter cloud observations included at SGP. We compare both sites and investigate how consistent the differences we observe are with other types of measurements.

2. Instruments and Data

[8] The SGP and SIRTA sites host ground-based lidar systems that measure the returned signal in both the parallel and perpendicular linear polarization state, albeit with some differences in wavelength and instrument specifications. Both instruments are described here along with ancillary measurements used in this study.

2.1. The Raman Lidar at SGP

[9] The SGP site possesses a Raman lidar that transmits laser pulses into the atmosphere at 355 nm and receives backscattered energy at 387 nm (nitrogen band), at 408 nm (water vapor band), and at 355 nm for aerosols and clouds, with depolarization measurements at 355 nm [*Goldsmith et al.*, 1998]. The technical specifications of the instrument are given in Table 1. The nominal temporal and vertical resolutions for the data used in this study are 1 min and 39 m, respectively. The tilt of the laser beam is about 3°–5° off nadir [*Wang and Sassen*, 2001]. The Raman lidar is housed in an environmentally controlled shelter, viewing the atmosphere through a window, and thus is able to profile throughout the diurnal cycle. The lidar has operated nearly continuously (with occasional periods of downtime due to laser failure), but the ARM archive only holds consistently processed data up to 2003 because an upgrade of the detection electronics in 2004 interfered with the processing of later data until recently [*Newsom et al.*, 2009]. Consequently, five winters were studied here, from November 1998 to March 2003, for a total of about 2085 h of observations.

Table 1. Specifications of SGP Raman Lidar and SIRTA LNA

Component	Characteristics	SGP Raman Lidar	SIRTA Lidar Nuages Aerosols
Transmitter	Wavelength	Linearly polarized 355 nm	Linearly polarized 532 nm, unpolarized 1064 nm
	Laser	Nd:YAG third harmonic	Nd:YAG second harmonic
	Energy/pulse	300–320 mJ	160 mJ
	Repetition rate	30 Hz	20Hz
	Tilt off nadir	3–5°	2–3°
Receiver	Diameter	61 cm	60 cm (narrow FOV), 20 cm (wide FOV)
	Detection channels used in this study	Cross-polarized and copolarized channels at 355 nm, Raman backscatter due to nitrogen at 387 nm	Cross-polarized and copolarized channels at 532 nm
	Channel band pass	0.4 nm	2.5 nm
	Filter transmission	30–40%	55%
	FOV	Narrow FOV 0.3 mr (used here) and wide FOV 2 mr	0.5 mr (narrow FOV), 5 mr (wide FOV)
	Range resolution	39 m	15 m
	Temporal resolution	1 min summed to 5 min	30 s averaged to 5 min

2.2. The Lidar Nuages Aerosols at SIRTA

[10] Cloud observations at SIRTA [*Haeffelin et al.*, 2005] are performed using the Lidar Nuages Aerosols (LNA), a dual-wavelength (532 and 1064 nm) zenith pointing Nd-YAG pulsed lidar. The 532 nm channel is linearly polarized. All lidar characteristics can be found in Table 1. The nominal temporal and vertical resolutions are 30 s and 15 m, respectively. The laser is also tilted off nadir by about 2°–3°.

[11] The SIRTA lidar observations are restricted to non-precipitating periods, as there is no environmental protection for the instrument. Consequently, the lidar is only operational during the daytime hours, 5 days a week (one seventh of the time according to *Protat et al.* [2006]). *Protat et al.* [2006] explored the impact of the discontinuous sampling on the cloud property statistics and found that, as long as the sampling is regular, it does not have to be continuous to sample all possible situations. However, the attenuation of the lidar beam causes a bias toward situations either clear or of low water content and no precipitation.

[12] For this study, five winters were available from November 2002 to March 2007, for a total of about 535 h of observations.

2.3. Additional Ground-Based Measurements

[13] Temperature profiles were obtained from soundings at both locations. At SGP, radiosondes are launched 3–8 times a day. For SIRTA, radiosonde profiles are available twice daily from the nearby Météo-France station of Trappes, about 15 km from the site. The same temperature profile is used for all lidar time steps within ±6 h of the radiosonde launch or less, if launches occur more frequently. Variations in temperature over a 6 h period, as obtained from reanalysis temperature profiles, are less than 1 K on average. The largest variations are found during frontal passages; however, in these cases, the clouds are usually optically thick and thus not included in this study.

[14] At SGP, the Active Remotely Sensed Cloud Locations data set [*Clothiaux et al.*, 2000] was used to derive the cloud top height estimated from the 35 GHz millimeter-wave cloud radar measurements [*Moran et al.*, 1998], as well as the maximum radar reflectivity within the cloud. Also, atmospheric column liquid water path (LWP) retrievals from nearby microwave radiometer measurements were extracted from the improved microwave radiometer retrievals of cloud liquid water and precipitable water vapor (MWRRET) data product [*Turner et al.*, 2007].

3. Lidar Profile Processing

[15] The two lidars have different temporal resolutions, so the raw profiles were summed at SGP and averaged at SIRTA to obtain a 5 min resolution for both data sets. This increases the signal-to-noise ratio in the lidar profiles. The different wavelengths at which the two lidars operate and the different extents to which the data have previously been processed to detect clouds present a challenge for cloud phase definition. The approach we used at the two sites is described below.

3.1. Depolarization Ratio Calculation and Cloud Masking

[16] At both sites, the total depolarization ratio is calculated as the ratio of perpendicular to parallel signals. The depolarization ratio is calibrated to give a value of 0.02 (2%) in cloud and aerosol-free areas where only the molecular contribution can be measured [see, e.g., *Sassen and Benson*, 2001]. This value is somewhat arbitrary, but the estimate of the real value depends on the instrument characteristics and is a complex operation that has not been performed at either site.

[17] The same elaborate cloud mask, Structure of the Atmosphere (STRAT) [*Morille et al.*, 2007], is applied to the elastic backscatter signal from both lidars to identify the content of each lidar bin: clear (molecular signal only), cloudy, aerosols, or noise. The "noise" flag characterizes bins where the signal-to-noise ratio falls below 3 and indicates significant beam attenuation. The cloud mask was treated with image processing erosion and dilation tools [e.g., *Gonzalez and Woods*, 1992] to avoid erroneous detections of isolated bins and to correct for sudden drops in depolarization near cloud edges.

[18] The SGP lidar data do not include a correction for the incomplete overlap of the outgoing beam with the detector's

field of view (FOV), which affects the accuracy of the signal in the bins close to the receiver [*Turner et al.*, 2002]. Consequently we ignored the first kilometer above the surface and removed any cloud that would have a base in the bin immediately above the 1 km limit.

3.2. Cloud Profile Selection

[19] We removed all cloud profiles that are fewer than three bin thick so that we can study the cloud phase at three distinct levels (base, median, and top). This means that at SGP all clouds are at least 117 m thick. Clouds of smaller extent constitute only 4% of all cloud profiles at SGP and are mostly found just above 1 km altitude where the overlap problem mentioned previously affects the quality of the measurements. Once these are removed, there are 28,820 cloud profiles in our data set at SGP. At SIRTA, the vertical resolution is higher, but for consistency with the SGP data set, we remove all clouds less than 120 m thick (at least eight bins). We will later see that the removal of thinner clouds has no effect on our results. These geometrically thin clouds constitute about 7% of all cloud profiles, leaving a total of 9606 cloud profiles at SIRTA.

[20] The main problem with using lidars to characterize cloud properties is laser beam attenuation in opaque clouds, which means that the cloud top cannot be detected by the lidar. Since we are interested in a full phase profile from cloud base to top, we discard all cloud profiles where the lidar signal-to-noise ratio falls below 3 at or below the lidar-identified cloud top [*Morille et al.*, 2007]. Also, low-level clouds cause problems for signal calibration, as there are not enough clear lidar bins below cloud base and they often attenuate the beam so there are no clear bins above the cloud either. These cases are automatically eliminated at the calibration stage at SGP. As an additional precaution at SGP, we use the 35 GHz radar cloud mask to remove any remaining lidar cloud profile that has a cloud top below that indicated with the radar.

[21] Overall, at SGP, 22,567 five minute cloudy profiles (~78% of all profiles containing cloudy bins) remain after the attenuation tests are applied and 21,770 (76%) remain after cloudy profiles with problems in depolarization ratio and temperature measurements (e.g., bad radiosonde temperature profiles) are removed. These profiles cover a total of 1892 h for the 327 days when data were available.

[22] At SIRTA, the lack of measurements in periods of precipitation removes mostly thick clouds that can attenuate the lidar beam, so fewer than 1% of the cloud profiles are removed with the attenuation test. However, this also limits severely the amount of time with measurements (nights, weekends, and holidays are excluded), giving 9525 five minute cloud profiles. Problems with the depolarization and temperature measurements further reduce the number of cloud profiles to 9279, which cover a total of about 480 h for the 112 days when data were available.

4. Phase Determination

[23] Cloud phase determination from lidar relies on the difference in depolarization effect between liquid droplets and ice crystals [*Sassen*, 1991]. Both lidars transmit polarized laser pulses, and ice crystals depolarize the backscattered energy, creating a nonnegligible ratio of perpendicular to parallel polarization signals, while spherical water droplets return a nearly zero depolarization ratio value in the 180° backscatter direction. When ice crystals and liquid droplets are found in the same lidar volume, low depolarization ratios are also found, unless the ice water content is much greater than the liquid water content or the ice crystals are small.

4.1. The Phase Determination Algorithm

[24] The radiosonde temperature profile is first used to categorize lidar cloud bins as only liquid (only ice) when the temperature is above 273 K (less than 233 K) [e.g., *Pruppacher and Klett*, 1997]. In the transition region, the depolarization ratio is used to separate liquid from ice. Figure 1 shows two examples, one for each site, of in-cloud depolarization ratios (Figures 1a and 1b), lidar attenuated backscatter (Figures 1c and 1d), and the corresponding phase retrievals (Figures 1e and 1f) obtained by using a depolarization ratio δ = 11% to separate liquid from ice (which we will refer to as the D-11 method), as suggested by *Intrieri et al.* [2002].

[25] The frequency of occurrence of depolarization ratio for SGP lidar bins colder than 233 K or warmer than 273 K is shown in Figure 2a. The shape of the distribution is very different depending on whether the bins contain ice ($T <$ 233 K) or liquid ($T >$ 273 K), and these two distributions indeed intersect at about δ =11%. The distributions are very similar at SIRTA (Figure 2b). There are some issues created by using a single threshold on depolarization ratios though. Figure 2 shows that about 5% at SGP and 11% at SIRTA of the clouds warmer than 273 K, which must be liquid, have $\delta >$ 11%. Furthermore, the distribution of depolarization ratio for $T <$ 233K (pure ice) is broad, with a peak near 20–30% but with ~12% of the lidar bins below the 11% threshold.

[26] Previous studies have shown that multiple scattering in liquid clouds can induce significant depolarization ratios, as the lidar beam travels through the cloud [e.g., *Sassen and Petrilla*, 1986; *Sassen et al.*, 1992; *Hu et al.*, 2001; *Noel et al.*, 2002]. This effect was found to increase with the lidar beam FOV, the cloud receiver distance and the liquid water content. However, both lidars here have small FOVs (see Table 1), and the small cloud optical thicknesses also reduce this effect. *Sassen et al.* [1992] show that with a 1 mrad FOV, the maximum depolarization ratio in pure liquid clouds does not exceed 0.25 at warm temperatures ($T = -10$°C), and *Ansmann et al.* [2009] find a maximum of 0.15 for similar clouds; thus, we are fairly confident that errors in phase determination caused by multiple scattering are small here, as illustrated by the small percentage of liquid clouds with large depolarization ratios. *Sassen and Petrilla* [1986] also suggest the influence of aerosol scavenging near cloud base may result in an increase in depolarization (aerosols do have a depolarization effect). The problem of small depolarization ratios in ice clouds occurs more often than large depolarization ratios in liquid clouds. Low values of depolarization ratios can be caused by particle shapes close to spherically [e.g., *Noel et al.*, 2006] or horizontally aligned crystals [e.g., *Platt* 1977; *Sassen* 1980; *Noel et al.* 2001; *Noel and Sassen,* 2005]. The latter is largely avoided by tilting the laser beam off nadir at both sites. As shown by *Sassen and Benson* [2001], a tilt of 2.5° or 4° corrects for specular reflection of horizontally aligned crystals in a similar fashion at tem-

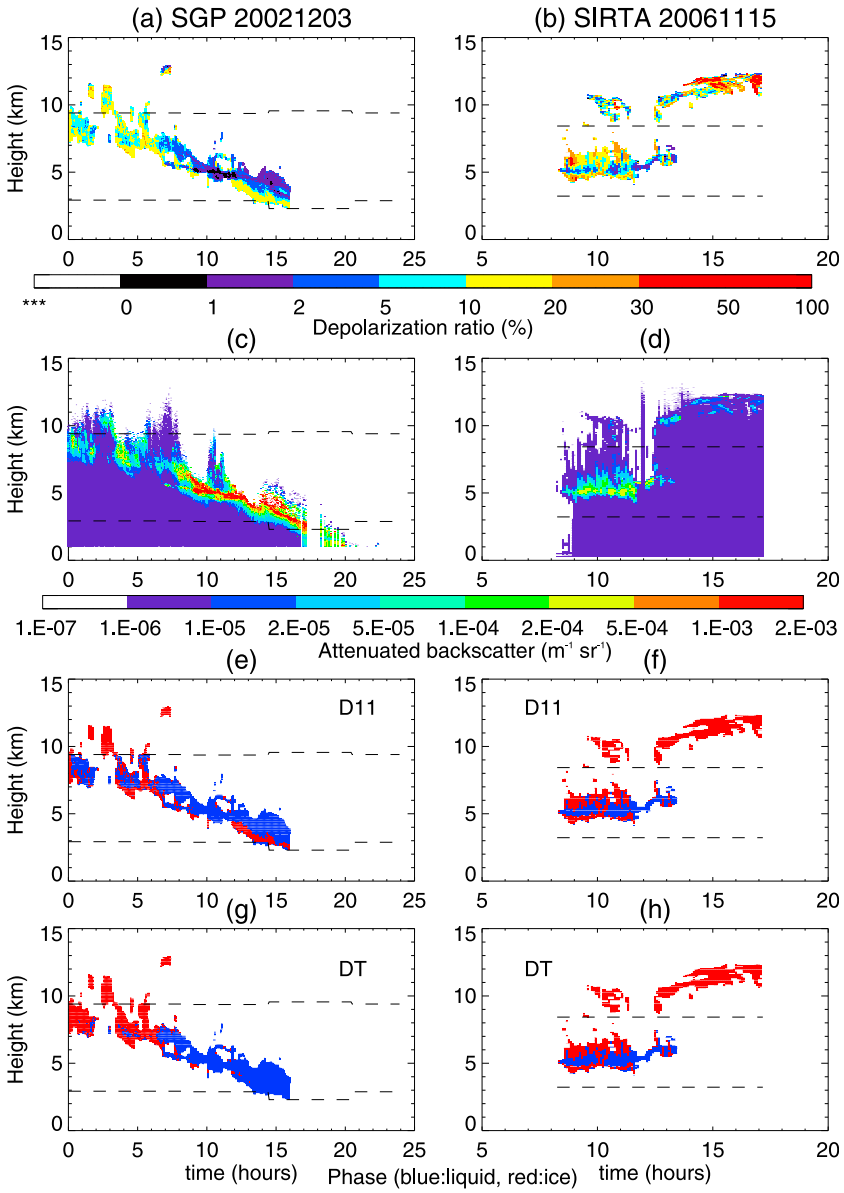

Figure 1. Depolarization ratio as a function of time and altitude in clouds detected with STRAT [*Morille et al.*, 2007] from (a) the SGP Raman lidar on 3 December 2002 and (b) the SIRTA LNA on 15 November 2006. Corresponding (c, d) lidar backscatter, (e, f) D-11, and (g, h) DT phase determination (see section 7.3) are shown for SGP and SIRTA, with blue lidar bins representing liquid retrieval and red bins representing ice retrievals. The dashed lines show the altitude of the 233 and 273 K levels for those days.

peratures between 273 and 233 K. We will discuss the implication of these problems for our results and possible correction in section 7.

[27] The joint distribution of lidar cloud observations at SIRTA and SGP as a function of δ and T is shown in Figure 3. Two distinct populations exist: one at low depolarization ratios ($\delta < 15\%$) and relatively warm temperatures (approximately 250–280 K) and the other at colder temperatures (200–240 K) and over a broad range of depolarization ratios ($\delta \sim 10$–50%). The SIRTA data set (Figure 3a) displays a much wider range of temperatures for the cold clouds than the SGP data set (Figure 3b) for a similar range of depolarization ratios. It is unclear if the larger occurrence of clouds with temperatures below 220 K at SIRTA is because these clouds are rare at SGP or because the Raman lidar at SGP is not sensitive enough to these clouds. It is also possible that the colder clouds are at higher altitudes at SGP where there is a greater chance that the signal-to-noise ratio falls below 3 before cloud top, and thus, these clouds are not included in the data set studied here. An interesting feature in Figures 3a and 3b is a tendency for cloud bins with a temperature less than 250 K to display an increase in depolarization ratio as temperature decreases. This is in agreement with *Sassen* [1991, Figure 7] and *Cho et al.* [2008]. *Noel et al.* [2006] find that in midlatitude ice cloud particle aspect ratios increase with

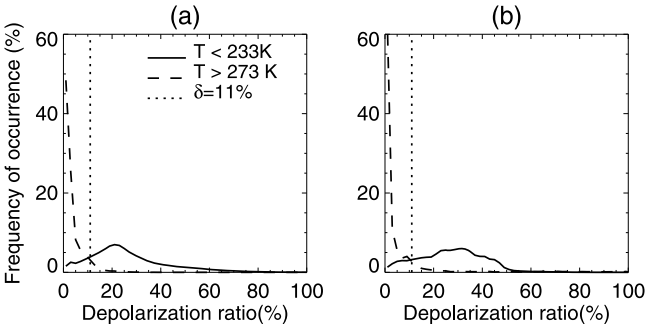

Figure 2. Distribution of depolarization ratios at (a) SGP and (b) SIRTA for all lidar bins of temperature < 233 K (solid) and > 273 K (dashed), with the depolarization ratio = 11% (dotted).

decreasing temperature, which causes an increase in depolarization ratios.

[28] The overall cloud layer phase can be obtained from the ratio of the number of ice lidar bins to the total number of bins in the cloud profile. This ice phase ratio varies between 0 for a pure liquid cloud and 1 for a pure ice cloud, with mixed phase clouds defined as those clouds where the ice phase ratio is fractional. Consequently, although each lidar bin cannot be considered as a mixed phase volume, a cloud composed of multiple bins can be considered a mixed phase volume, defined here as the vertical extent between cloud base and cloud top in a 5 min profile; this follows the same logic that was used by *Shupe et al.* [2008].

4.2. Evaluation of the Phase Determination Method

[29] To assess the strengths and weaknesses of this method, we compared the D-11 cloud phase at SGP with independent MWRRET (see section 2.3) LWP retrievals [*Turner et al.*, 2007]. We examined whether ice phase clouds are detected when the MWRRET LWP was greater than 30 g m^{-2}, the approximate detection limit for the microwave radiometer [*Turner et al.*, 2007]. Clouds of low optical thickness will have a low LWP, so about 8% of all unattenuated cloud profiles at temperatures warmer than 233 K have LWP > 30 g m^{-2}. When LWP > 30 g m^{-2}, the D-11 method identified 65% of the clouds as liquid, 34% as mixed phase, and only 1% as ice.

[30] Other methods have been proposed in the literature to derive cloud phase from lidar depolarization ratios, but usually in association with other instruments, e.g., to allow phase determination in optically thick clouds, which makes them difficult to implement at multiple sites that may not possess the same instruments [e.g., *Wang and Sassen*, 2001; *Shupe et al.*, 2006]. *Wang and Sassen* [2001; hereafter referred to as WS01] derive the overall cloud phase (from cloud base to top) by using a threshold on the maximum total depolarization ratio and the value of the scattering ratio (SR), as well as the value of the maximum 35 GHz radar reflectivity. In addition, they use the MWR LWP information to confirm the presence of liquid water. We applied the WS01 method to the SGP observations. When MWRRET LWP is greater than 30 g m^{-2}, the WS01 method indicates liquid cloud in 74%, mixed phase in 23%, and ice phase in 3% of all cloud profiles. A comparison between WS01 and the D-11 method was performed, assuming that a cloud with a D-11 ice phase ratio between 0 and 1 can be considered as a mixed phase cloud (Table 2). For all cloud profiles with a median temperature between 233 and 273 K, the D-11 method determined that 35% were pure liquid, 44% were a mixture, and 21% were pure ice, while WS01 determined that 30% were pure liquid, 15% were a mixture, and 54% were pure ice. These different statistics partially come from a tendency for the D-11 method to detect pure liquid clouds when ice crystals may be present, as revealed by coincident large 35 GHz radar reflectivities; that is, radars are more sensitive to large ice crystals (even if there are relatively few in number) than many small liquid droplets, and for these cases, the radar reflectivity exceeded −20 dBz (pure liquid in nondrizzling clouds would give reflectivities well below this threshold). For these cases,

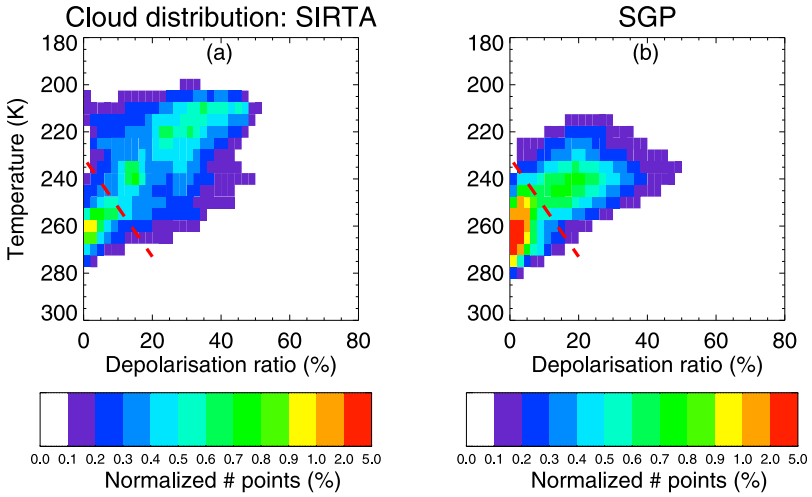

Figure 3. Number of cloudy bins in 2 K temperature and 2% depolarization ratio intervals normalized as a percentage of the total number of cloudy bins in unattenuated profiles for all winter months (a) from 2002 to 2007 at SIRTA and (b) from 1998 to 2003 at SGP. The red dashed line shows the temperature-dependent separation threshold chosen to differentiate liquid from ice bins, with ice above the line where the depolarization ratios are largest and temperatures are coldest (see section 7.3).

Table 2. Percentage of Cloud Observations at the SGP With Median Temperatures Between 233 and 273 K According to the WS01 and D-11 Phase Determination Methods

WS01	D-11 Liquid	D-11 Mixed	D-11 Ice
Liquid	22	6	<0.5
Mixed	7	8	<0.5
Ice	6	30	20

WS01 determined that the clouds were in mixed phase because they also use a test based on radar reflectivity. It also indicates a tendency for WS01 to detect ice clouds that, in fact, are mixed phase clouds, which is slightly corroborated by the larger proportion of pure ice clouds detected by WS01 when MWRRET LWP indicates the presence of liquid in the cloud. Figure 4 illustrates how the cloud median-level temperature of the three cloud types (liquid only, mixed phase, and ice only) is distributed when normalized to the total number of cloud profiles using the two methods at SGP and with the D-11 method only at SIRTA. Figures 4a and 4b show that D-11 and WS01 agree fairly well when temperatures are warmer than 255 K (albeit with relatively more mixed than liquid phase clouds for WS01) but differ at cold temperatures, where WS01 determines that all clouds are ice below 245 K while D-11 gives a large occurrence of mixed phase clouds. Figures 4a and 4c show that the temperature distributions for the three cloud phases are fairly similar between SGP and SIRTA, with a larger relative occurrence of mixed phase clouds and fewer liquid clouds at warm temperatures at SIRTA.

5. Cloud Properties at SIRTA and SGP

[31] In this study, cloud phase detections are retained when the optical thickness is low enough to avoid lidar beam attenuation. Consequently, not all cloud types are sampled and the range of dynamic situations is limited. For those times when unattenuated cloud profiles could be obtained, the nearest low-pressure center found in the Modeling, Analysis, and Prediction Climatology of Midlatitude Storminess (MCMS; http://gcss-dime.giss.nasa.gov/mcms/mcms.html) data base was obtained. Figure 5 shows the distribution of the position of the SGP and the SIRTA cloud observations relative to the nearest low-pressure center. At SGP, the clouds are usually situated immediately north or west/southwest of the low, while at SIRTA, the clouds are most often southeast of the low, with a secondary maximum over a broad region west of the low. According to the composite vertical motion pattern of baroclinic storms, at these distances and in these directions, when clouds are observed, the sites are generally found in the subsidence and cold advection zones of midlatitude cyclones or in the warm sector in advance of a cold front [*Naud et al.*, 2006, Figure 8].

[32] At both sites, we separate mixed phase clouds into two categories: (1) those with ice at cloud top and (2) those with liquid at cloud top (regardless of how phase is distributed at lower cloud levels). There are more clouds of uniform phase at SGP than at SIRTA, and at both sites, more mixed phase clouds have ice rather than liquid at cloud top, the difference being greater at SIRTA than at SGP (Table 3). Overall, ~15% of the clouds we observed at both locations and fewer than half of the mixed phase clouds have a supercooled liquid droplet layer at cloud top (category b in Table 3). It was observed in the Arctic for a wider range of cloud optical thickness that half of the mixed phase clouds observed during a year of ground-based observations showed a liquid layer at cloud top [*Shupe et al.*, 2006]. Supercooled cloud tops are apparently easily maintained in the Arctic because of the dearth of ice nuclei there [*Fridlind et al.*, 2007], while SIRTA, for example, is in a populated continental region in which anthropogenic aerosols that can nucleate ice may be much more prevalent than in the polar region.

[33] The average cloud median altitude (the altitude of the lidar bin closest to the geometrical center of the cloud), thickness, and lapse rate are given in Table 4 for clouds in liquid, mixed, and ice phase determined with the D-11 method, while Table 5 gives the same averages for the mixed phase clouds separated according to the two categories defined above. Clouds are generally found at slightly higher altitudes at SGP than SIRTA (see Table 4), and the distribution of median heights (Figures 6a and 6d) indicates that pure liquid clouds are on average higher at SGP (recall that clouds with a base below or at 1 km were removed from the SGP data set, but not from the SIRTA data set). Mixed and ice phase clouds at SGP show a peak in frequency of occurrence at higher altitudes than at SIRTA. At both sites,

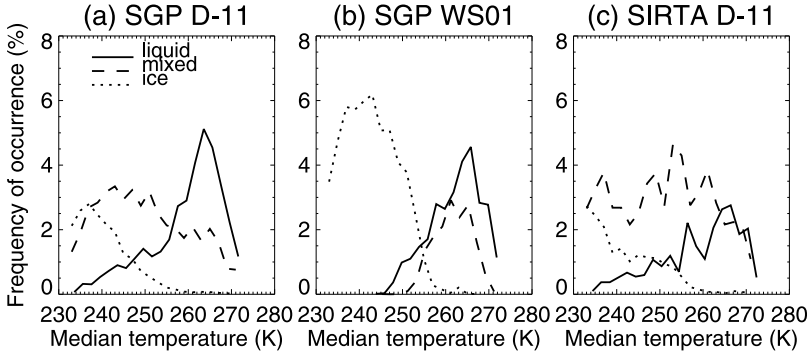

Figure 4. Cloud median temperature distribution at SGP (a) using the D-11 method and (b) using WS01 and (c) at SIRTA using the D-11 method for pure ice clouds (dotted), mixed clouds (dashed), and pure liquid clouds (solid), normalized to the total number of cloud profiles collected at each site with no lidar attenuation.

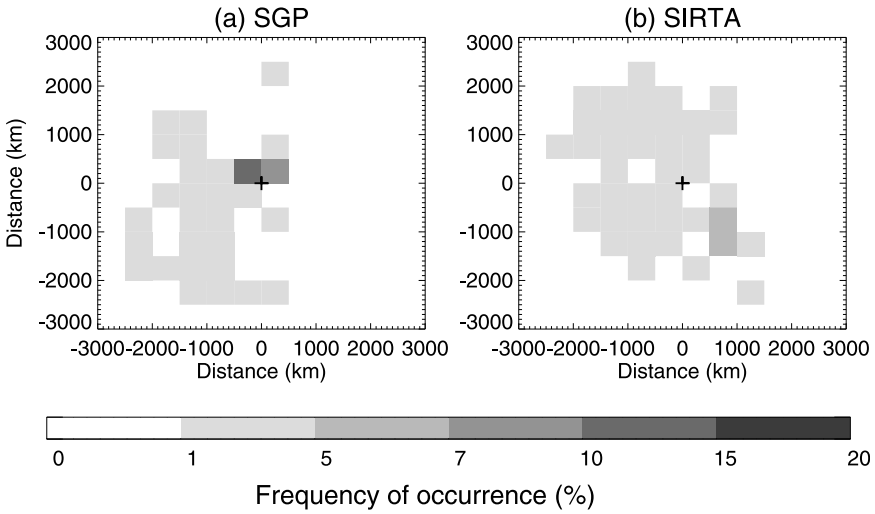

Figure 5. Frequency of occurrence (%) of the position of the SGP and SIRTA cloud observations with respect to the location of the closest coincident low surface pressure center available in the MCMS data base, represented in a 2500 × 2500 km^2 zone centered on the low and calculated in equal area 500 × 500 km^2 grid cells normalized to the total number of unattenuated cloud profiles.

mixed and ice phase clouds cover a greater vertical extent than the liquid cloud types, probably because thick liquid clouds attenuate the lidar beam and are excluded from our analysis here (see Table 4). There are more mixed phase clouds of extent greater than 1.5 km than for the other two cloud types at SGP, but at SIRTA, mixed and ice phase clouds have similar extents (Figures 6b and 6e). The lapse rate distributions are similar at both sites with steeper rates, as clouds are found at higher altitudes (Figures 6c and 6f). Mixed phase clouds with ice at cloud top tend to be slightly higher than the other types at both locations, but differences in thickness and lapse rates are marginal (see Table 5 and Figure 7).

6. Relationship Between Ice Phase Occurrence and Temperature

[34] Phase and corresponding temperatures are collected for three distinct cloud levels identified in each individual unattenuated 5 min lidar cloud profile: cloud base, cloud top, and in the bin at median height between base and top. For each level, the profiles are grouped according to the temperature at that level, from 233 to 273 K in 4 K bins. For each temperature bin, the ratio of the number of profiles with ice phase at the level in question to the total number of profiles in the temperature bin is calculated. This ratio is called the ice phase frequency of occurrence.

[35] The D-11 ice phase occurrence versus temperature relationship at cloud base, median, and top at both sites is presented in Figures 8a and 8b. The variability in ice phase occurrence increases as temperatures increase due to the lower number of profiles with a cloud top temperature close to 273 K, which explains the slight rebound in the cloud top curve in Figures 8a and 8b. There are on average 1400 points per temperature bin in the SGP data set and about 350 in the SIRTA data set, but at both locations, this number significantly decreases for temperatures warmer than about 260 K. At SGP, ice phase occurrence is very similar at cloud top and median levels, but cloud base differs with a greater chance of ice to be present than at the other levels, possibly due to ice precipitation. However, because of the large number of clouds with a uniform phase at SGP, the difference between the three levels is strongly influenced by the difference in temperature between the three levels (with cloud base warmer than median, itself warmer than cloud top). At SIRTA, the three levels show very similar behaviors at intermediate temperatures.

[36] The distribution of ice phase occurrence as a function of temperature in mixed phase clouds at the two sites is shown in Figure 9. At SGP (Figure 9a), the relation between ice phase occurrence and temperature is similar to that for

Table 3. Distribution of Cloud Observations at Both Sites According to D-11 Cloud Phase in the 233–273 K Temperature Range

Cloud Phase	Fraction of Optically Thin Clouds (%)	
	SGP	SIRTA
Uniform (liquid and ice)	57	42
Uniform (ice)	21	20
Uniform (liquid)	36	22
Mixed (all)	43	58
(a) Ice at cloud top	26	43
(b) Liquid at cloud top	17	15

Table 4. Average Cloud Median Height, Vertical Thickness, and Lapse Rate at Median Level for SGP and SIRTA Liquid, Mixed, and Ice Clouds Found in the 233–273 K Temperature Range According to the D-11 Method

Average per Subset	SGP			SIRTA		
	Liquid	Mixed	Ice	Liquid	Mixed	Ice
Median height (km)	4.3	6.1	7.7	3.7	5.5	7.0
Thickness (km)	0.6	1.2	1.0	0.4	1.0	1.1
Lapse rate (K km^{-1})	6.6	7.1	7.7	6.4	6.8	7.5

Table 5. Same as Table 4 but for Mixed Phase Clouds Only According to the D-11 Method[a]

	SGP		SIRTA	
Average per subset	a	b	a	b
Median Height (km)	6.3	5.8	5.6	5.1
Thickness (km)	1.2	1.2	1.1	0.9
Lapse rate (K km^{-1})	7.2	7.0	6.9	6.6

[a]For clouds with (a) ice at cloud top and (b) liquid at cloud top.

uniform clouds in the 250–260 K temperature range, with a much larger ice phase occurrence at cloud base than median. Since the occurrence of mixed phase clouds with ice at cloud top is larger than for liquid-topped clouds, the similar relationship to Figure 8a at cloud base and cloud top for intermediate temperatures at SGP suggests that, when ice is present at cloud top, it is sometimes also present at cloud base, i.e., liquid layers are found within the cloud. At SIRTA (Figure 9b), the relationship between ice phase occurrence and temperature is similar to SGP at median level, but the relationship at cloud top is overridden by the much greater occurrence of ice-topped than liquid-topped clouds (Table 3). This causes the ice phase occurrence to be systematically higher at cloud top than at the other levels for all temperatures, except for the range 235–245 K. At cloud base, liquid seems to persist to colder temperatures at SIRTA than SGP. Because ice occurrence at cloud base may be related to ice sedimentation, the difference between the two sites may indicate that ice sedimentation in optically thin winter clouds is more active at SGP, maybe because ice crystals grow faster or larger there.

[37] Finally, Figures 8a and 8b indicate a general tendency for liquid to be present at colder temperatures at SGP than at SIRTA at cloud top and median levels. The temperature at median level for which ice phase occurrence reaches 50% (T_{50}) is 254 K at SIRTA and 248 K at SGP for all cloud profiles. The difference in T_{50} between the two sites (ΔT_{50}\{SIRTA-SGP\}) is +6 K, indicating a tendency for liquid to stay supercooled to colder temperatures at SGP than SIRTA. Note that at cloud base, in contrast, ΔT_{50}\{SIRTA-SGP\} is −1 K.

7. Sensitivity Study

[38] Because of the different systems used at both sites and the various assumptions that had to be made along the way, we checked the impact on the difference in T_{50} at median cloud level between the sites ΔT_{50}\{SIRTA-SGP\} of the size of the data sets and the choice of minimum cloud extent at SIRTA, the choice of the SGP cloud mask, the choice of total depolarization rather than particle depolarization at SGP, and the choice of the phase determination method.

7.1. Sensitivity to Cloud Profile Sampling

[39] The SIRTA data set is about a quarter as large as the SGP data set, so we randomly reduced the size of the SGP data set and calculated ΔT_{50}\{SIRTA-SGP\}. We find ΔT_{50}\{SIRTA-SGP\} ranging from +3 K to +9 K.

[40] If we include in the SIRTA data sets clouds with between three and eight bins, ΔT_{50}\{SIRTA-SGP\} = +5 K. In other words, there is little change.

7.2. Sensitivity to Cloud Mask and Depolarization Ratio

[41] All the results presented in this study are using the STRAT cloud mask; however, the sensitivity of our statis-

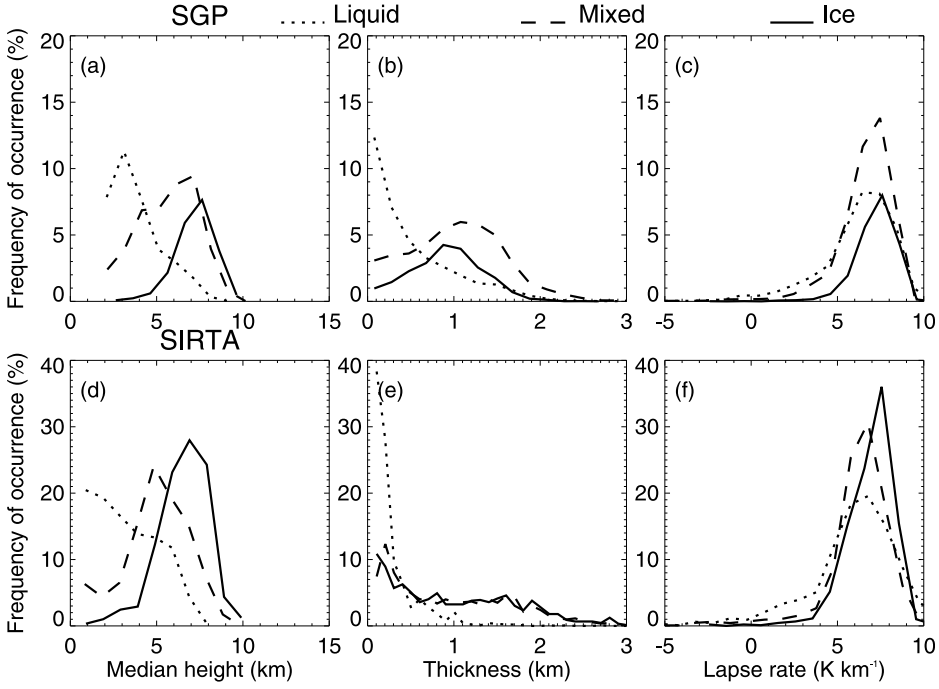

Figure 6. Frequency of occurrence of cloud median height, thickness, and lapse rate at median level for liquid (dotted), mixed (dashed), and ice (solid) clouds observed at (top) SGP and (bottom) SIRTA and using the D-11 method for phase determination.

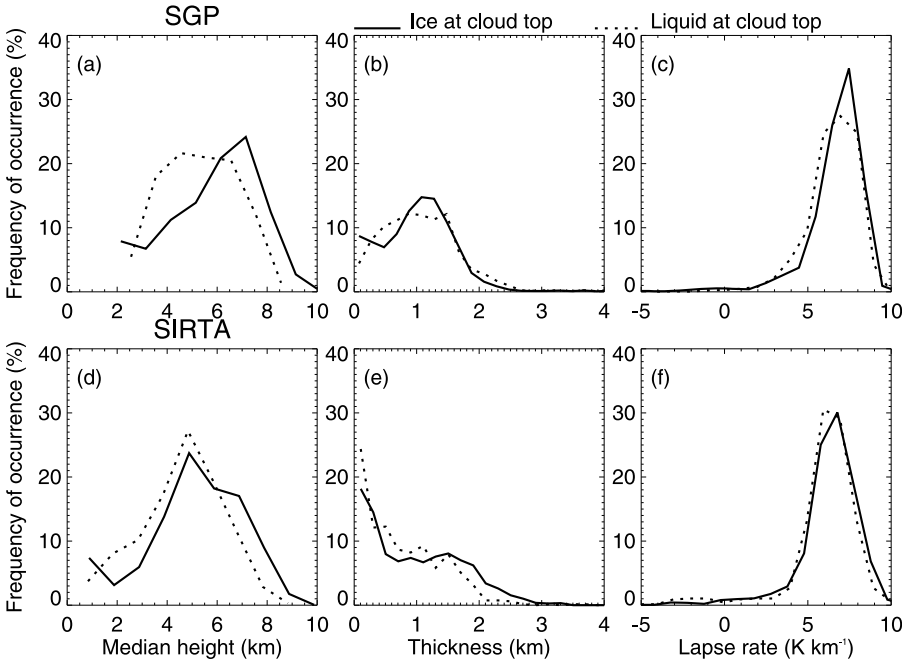

Figure 7. Same as Figure 6 for mixed phase clouds that have (a) ice at cloud top (solid) and (b) liquid at cloud top (dotted) observed at (top) SGP and (bottom) SIRTA.

tical results to the choice of cloud mask is examined by using an operational ARM Raman lidar cloud mask [*Turner et al.*, 2002]. With their method, clouds are detected when the SR is greater than 5 below 5 km and greater than 3.5 above 5 km [*Turner et al.*, 2002]. Also, above 5 km, a volumetric depolarization ratio of more than 7% is also assumed to indicate clouds for those pixels where SR < 5. When the cloud mask at SGP is replaced with the mask proposed by *Turner et al.* [2002], ΔT_{50}{SIRTA-SGP} = +5 K. Again, the change is very small.

[42] The total (or volumetric) depolarization ratio includes both cloud and molecular contributions, making it difficult

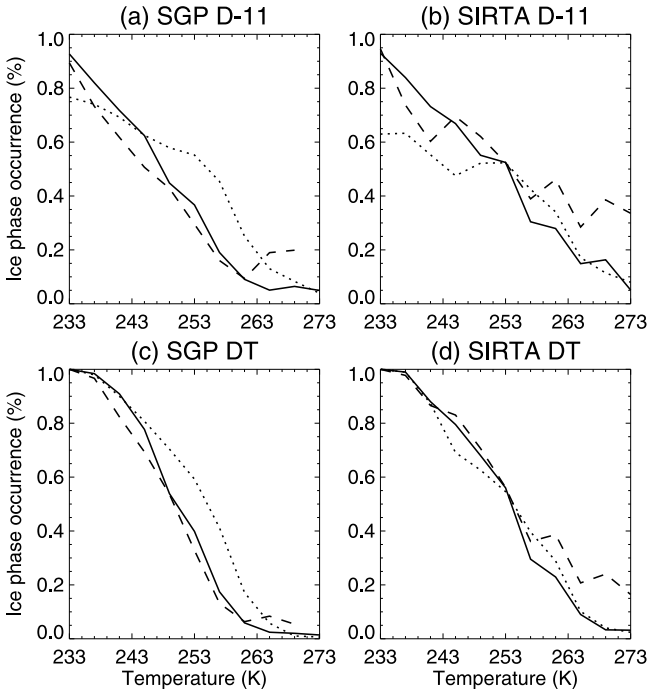

Figure 8. Ice phase occurrence versus temperature at cloud top (dashed), median level (solid), and base (dotted) for all clouds between 233 and 273 K (a) at SGP (17,177 profiles) and (b) at SIRTA (4415 profiles) using D-11 for cloud phase determination and same using DT (see section 7.3) at (c) SGP and (d) SIRTA.

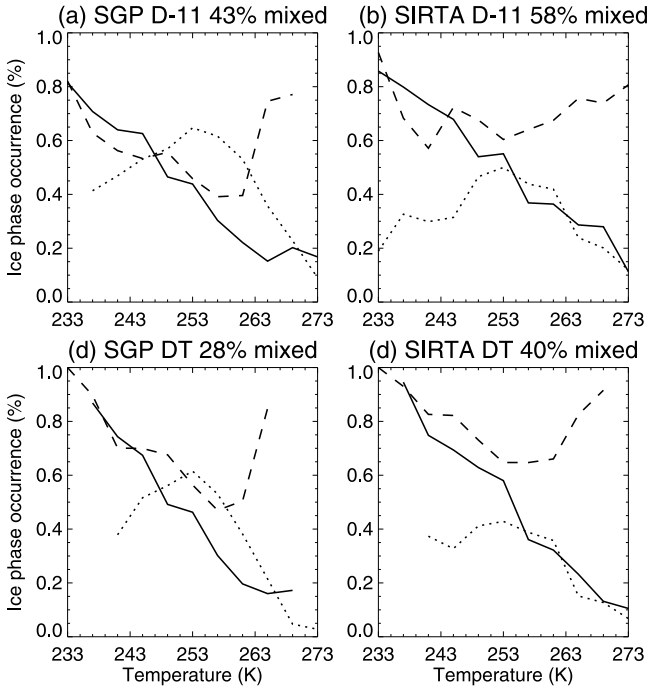

Figure 9. Same as Figure 8 but for mixed phase clouds only.

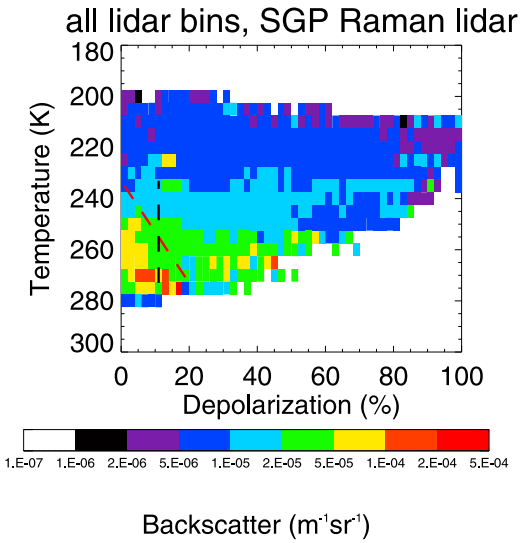

Figure 10. Average backscatter as a function of lidar bin temperature and depolarization ratio for the SGP data set. The black dashed line shows the 11% depolarization threshold, and the red dashed line indicates the temperature-dependent threshold on depolarization ratio used with the DT method.

to obtain a good cloud signal if the condensed water content is low. This is more so at the 355 nm SGP lidar wavelength than at the 532 nm wavelength of the SIRTA lidar, because the molecular contributions follow the λ^{-4} wavelength dependence of Rayleigh scattering. So for the purpose of sensitivity tests at SGP, the particle depolarization ratio is also calculated [*Murayama et al.*, 1999]:

$$\delta_{\text{particle}} = \frac{\text{SR} \times \delta_{\text{volumetric}} - 0.02}{\text{SR} - 1}, \qquad (1)$$

where the particle depolarization ratio δ_{particle} is extracted from the volumetric (total) depolarization ratio $\delta_{\text{volumetric}}$ once the molecular contribution (0.02) is removed using the SR (ratio of total aerosol plus molecular backscatter signal to molecular backscatter signal). Raman lidars such as the ARM system directly measure the molecular signal (the nitrogen Raman backscattered return), and thus, the ratio of the backscatter at the lidar wavelength (which has contributions from both aerosol and molecular scattering) divided by the nitrogen backscatter signal is proportional to the SR. When we use particle depolarization at SGP instead of total depolarization to avoid the contamination by molecular depolarization, $\Delta T_{50}\{\text{SIRTA-SGP}\} = +4$ K.

7.3. Sensitivity to Phase Determination Method

[43] In Figures 8a and 8b, as the temperature approaches 233 K or 273 K, the D-11 ice phase occurrence does not approach 1 or 0, suggesting a strong discontinuity at these two temperatures. In addition, we saw earlier that some liquid clouds exhibit depolarization ratios of >11% and some ice clouds have low depolarization ratios (<11%; Figure 2). Thus, we suspect that small depolarization ratios in ice clouds or large depolarization ratios in liquid clouds explain the discontinuities and we propose a simple way of correcting for this in order to test the sensitivity of our results to phase determination methods.

[44] *Sassen et al.* [1992] show that the magnitude of the multiple-scattering effect depends on several, sometimes interrelated, parameters, such as cloud receiver distance, the liquid water content, and the lidar FOV. It is thus complicated to find a simple method to compensate for these effects on phase determination, but there is some indication that multiple scattering is influenced by cloud temperature [*Sassen and Petrilla*, 1986]. Another problem we mentioned in section 4 is the low depolarization ratios that can occur in ice clouds. *Noel et al.* [2006] show that crystal shapes change with temperature, from platelike at warm temperature ($T <$ −20°C) to irregular (−40°C to −60°C) and then column-like ($T <$ −60°C) as temperatures decrease. At the same time, each shape exhibits a specific aspect ratio, which in turn implies a different range of depolarization ratios from $\delta < 0.25$ for platelike crystals to more than 0.5 for columns. This relationship between temperature and depolarization ratios can clearly be observed in Figure 3.

[45] Clouds composed of ice should display low attenuated backscatter and large depolarization, while clouds composed of liquid should display large attenuated backscatter and low depolarization. Figure 10 gives the average backscatter in each depolarization-temperature box displayed in Figure 3b for the SGP data set. Indeed, the backscatter increases significantly as the depolarization falls below 11% or when the temperature increases, but there are two regions of the diagram where this delineation is ambiguous: temperatures below 253 K with depolarization ratios of less than 11% display low backscatter, while warmer temperatures with depolarization ratios of greater than 11% can have large backscatter values.

[46] The dependence of the depolarization ratio distribution on temperature at SGP in 10 K temperature intervals is shown in Figure 11. The distributions change progressively as temperature increases. The 283–293 K distribution has no lidar bins with $\delta > 11\%$, while the 273–283 and 263–273 K distribution have less than 1% of lidar bins with $\delta > 13\%$ and $\delta > 20\%$, respectively. A calculation of the depolarization value that occurs 1% of the time for a bin centered on

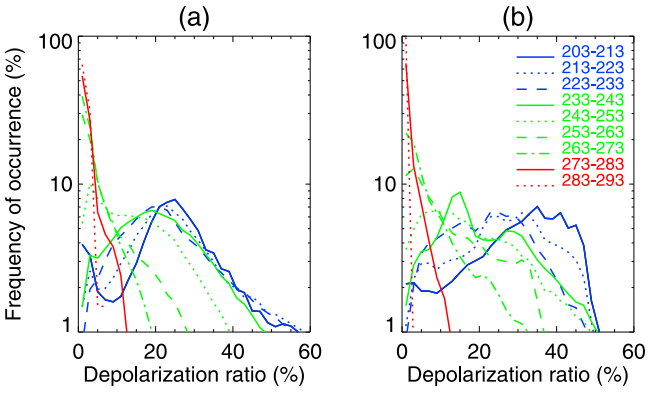

Figure 11. Same as Figure 2 but for lidar bins sorted in 10 K temperature bins with colder than 233 K in blue, between 233 and 273 K in green, and warmer than 273 K in red at (a) SGP and (b) SIRTA.

Table 6. Same as Table 3 but for the DT Method

Cloud Phase	Fraction of Optically Thin Clouds (%)	
	SGP	SIRTA
Uniform (liquid and ice)	72	60
Uniform (ice)	34	36
Uniform (liquid)	38	24
Mixed (all)	28	40
(a) Ice at cloud top	19	31
(b) Liquid at cloud top	9	9

273 ± 5 K gives 17%. In the 273–233 K temperature range, the depolarization distribution shifts progressively to larger values as temperature decreases. Figure 11 reveals that the largest change in distribution shape occurs in the transition from 253–263 K to 243–253 K. The 223–233 K distribution shows a significant amount of lidar bins with $\delta < 11\%$, while the 213–223 K and 203–213 K distributions show fewer than 2% of the lidar bins with $\delta < 11\%$.

[47] Consequently, we explore the sensitivity of our results to the choice of threshold using an alternative approach (which we will refer to as the DT method) with a threshold on depolarization ratio linearly changing with temperature to distinguish between ice and liquid lidar bins. The threshold dependence on temperature is based empirically on the distributions shown in Figure 10. The threshold at 273 K is chosen as 20%, slightly larger than the 11% suggested by *Intrieri et al.* [2002] to encompass all the liquid clouds in Figure 11. At 233 K, the threshold is chosen to be 0% to ensure continuity of phase in cold clouds as T decreases beyond 233 K, as also shown in Figure 2. The threshold decreases linearly from 20% to 0% as the temperature decreases from 273 to 233 K. Figures 1g and 1h show how the DT phase retrieval differs from D-11 for the examples introduced previously, identifying fewer liquid bins in the coldest portion of the clouds. For example, in Figure 1g, it can be noticed that the earlier hours at the SGP show clouds with low depolarization ratios but also low backscatter values; the D-11 method classifies these clouds as liquid at very low temperatures, whereas DT mainly identifies them as ice. Consequently, the DT method helps avoid some possible misidentification of liquid bins at cold temperatures and conversely helps identify some liquid bins of depolarization greater than 11%. We conducted a comparison of the phase obtained with the DT method with LWP retrievals and the WS01 methods as in section 4 and found results very similar to what we obtained with D-11 (not shown).

[48] The advantage of the D-11 method is its simplicity and wide usage. On the other hand, DT seems more consistent with backscatter identification of liquid and thus may correct some imperfections that result when using a single threshold, thereby allowing us to reclassify clouds that display ambiguous lidar volume depolarization signals but without affecting our conclusions at intermediate temperature. But more importantly, Figures 8c and 8d show how the discontinuity problem near 233 and 273 K is avoided by the DT threshold method (compared to Figures 8a and 8b) but without changing the overall relationship at intermediate temperatures. Similarly, Figures 9c and 9d show the same relationship for mixed phase clouds obtained using DT: the relationship at intermediate temperatures is similar whether D-11 or DT is used, but near the 233 and 273 K limits, DT does not show a jump in ice phase occurrence. Cloud frequency of occurrence values according to the phase obtained with DT are given in Table 6. Table 6 reveals, however, that D-11 and DT agree in their classifications of 80–85% of clouds, with DT detecting more pure ice and D-11 detecting more mixed phase.

[49] When we replace the D-11 method with the DT method at both locations, we find a tendency for the DT method to give slightly warmer T_{50} at the median cloud level, as expected, by 1–2 K. When we then compare the two sites, $\Delta T_{50}\{\text{SIRTA-SGP}\}$ becomes +4 K, which is only 2 K different from the same difference obtained with D11.

[50] Overall, the cloud median level T_{50} at SIRTA is always warmer than at SGP, regardless of the specifics of the phase determination. When we average T_{50} over all possible ways of processing the data and calculate the 1 sigma standard deviation, we find 254 ± 1 K at SIRTA and 248 ± 2 K at SGP.

8. Discussion and Conclusions

[51] Clouds of uniform phase are found in 57% at SGP and 42% at SIRTA of depolarization lidar observations of optically thin clouds when a constant (temperature-dependent) threshold for phase determination is used. Using aircraft observations in frontal systems between 42°N and 83°N from five distinct campaigns, *Korolev et al.* [2003] found clouds of uniform phase in 60–70% of their observations, depending on the temperature range, more than what we find at both sites for optically thin clouds when we determine the phase with a fixed threshold on depolarization ratio but similar to what we find when using a threshold that changes with temperature (Table 6). In the Arctic, however, for a wide range of optical thicknesses, *Shupe et al.* [2006] found uniform phase clouds to occur only 40% of the time, suggesting that mixed phase clouds at SGP may attenuate the lidar beam more often than clouds of uniform phase (in particular, ice clouds) or that dynamic and/or nucleation differences between the Arctic and the midlatitude optically thin winter clouds may be at play. Most of the mixed phase clouds we detect at both the SGP and SIRTA sites are ice topped, while ~15% of the clouds found within 233–273 K range have a liquid layer at cloud top. The change in the relation between ice phase occurrence and temperature as a function of cloud level is small at both sites and is influenced both by the mean temperature difference between base and top and by a preference for the mixed phase clouds to have ice at cloud top. Also, ice occurrence was found to be slightly larger at cloud base than at other cloud levels at SGP, suggesting that optically thin mixed phase clouds at this site tend to have more liquid within than at the boundaries. However, at SIRTA, ice occurrence decreased toward cloud base in mixed phase clouds. There is a possibility that sedimentation is more efficient at cloud base at SGP than at SIRTA.

[52] Both locations are in midlatitude regions of baroclinic instability and thus experience a variety of synoptic situations. However, given the limitations imposed by lidar attenuation, the clouds sampled here represent a complement to the optically thick clouds within frontal regions. Taking into account the different uncertainties inherent to

the data processing introduced here, the resulting relation between phase and temperature is fairly stable and consistent with previous results for phase and temperature at SGP obtained with a different instrument [*Riedi et al.*, 2001]. *Riedi et al.* [2001] found that, at SGP, ice and liquid clouds detected with Polarization and Directionality of the Earth's Reflectances (POLDER) [*Deschamps et al.*, 1994] have temperatures (as retrieved with radiosondes profiles and radar derived cloud top heights) either colder than 240 K for pure ice or warmer than 240 K for pure liquid clouds. This is consistent with the 234–244 K temperature (depending on the phase determination method and site) below which liquid is not found with the lidar (Figure 4) but for a wider range of cloud optical thicknesses. Both POLDER and this lidar study yield a colder T_{50} cloud top value, by at least 12 K, than the 266.5 K found by *Bower et al.* [1996], which was estimated within frontal clouds and is still used for the development [e.g., *Lopez*, 2002] or evaluation [e.g., *Rotstayn et al.*, 2000] of GCM parameterization schemes.

[53] These results complement the passive remote sensing cloud top observational constraint for microphysical processes in GCMs provided by *Naud et al.* [2006]. For optically thin clouds, not only at cloud top but also within cloud and at cloud base, liquid in clouds other than thick frontal nimbostratus can persist to significantly colder temperatures than the frontal clouds sampled by *Bower et al.* [1996]. The differences we find between the optically thin cloud subset used here and the earlier *Naud et al.* [2006] study (with a T_{50} at cloud top somewhat larger in the subsidence zone, see their Figure 11) suggest that thin clouds may not experience the same glaciation processes as thicker clouds, perhaps because of differences in the dynamics but also because these clouds may represent a specific stage in a cloud life cycle (e.g., on the verge of total dissipation).

[54] Cloud thermodynamic phase retrievals with depolarization lidars are still in their infancy. Full validation of phase determination methods has not yet been possible, and further evaluations are needed such as, for example, aircraft campaigns conducted through nonfrontal mixed phase clouds over the lidar sites. Nevertheless, here we show how an empirical method, DT, can be an improvement on the traditional D-11 threshold technique. In any case, the two methods agree on the phase of 80–85% of clouds in the mixed phase temperature range. Most importantly, both methods indicate that GCM liquid-ice partitioning should allow for the presence of liquid at much colder temperatures than has been assumed on the basis of the *Bower et al.* [1996] data set, in accordance with other aircraft campaigns [e.g., *Fleishauer et al.*, 2002, and references therein; *Field et al.*, 2004, Figure 17; *Carey et al.*, 2008] but for a much longer period of observations. In addition, ground-based observations should be consistent (i.e., use similar technologies and retrievals) from one location to another if they are to be useful for deriving climatological regional differences. This is not yet the case for the existing suite of ground-based lidars and radars. We recommend that the active remote sensing community work toward the adoption of uniform instrument and algorithm design to optimize these systems for climate research; some of these activities have already been initiated for aerosol research [e.g., *Matthais et al.*, 2004]. The launch of the Cloud-Aerosol Lidar and Infrared Pathfinder Satellite Observation [*Winker et al.*, 2007] satellite experiment and phase retrievals from its depolarization measurements should also help in this task by providing top-down global sampling to complement the bottom-up view of the ground-based lidars. Finally, as stressed at the beginning of this study, lidars are limited to observing optically thin clouds, so, although these observations fill in a gap in that other instruments such as radars may not be sensitive enough to detect these clouds, uncertainties remain about glaciation inside optically thick clouds. Radar spectra (that use Doppler velocities as a means to decide if crystals or drops are present above the radar) may be eventually used for this purpose, but at present such techniques are still in the development stage [*Shupe*, 2007].

[55] **Acknowledgments.** This work was supported by an Interagency Agreement with the Atmospheric Radiation Measurement program of the U. S. Department of Energy. Support for D. Turner was provided by grant DE-FG02-06ER64167 from DOE BER as part of the ARM program.

References

Ackerman, T. P., and G. M. Stokes (2003), The Atmospheric Radiation Measurement program, *Phys. Today*, *56*, 38–44.

Ansmann, A., M. Tesche, P. Seifert, D. Althausen, R. Engelmann, J. Fruntke, U. Wandinger, I. Mattis, and D. Müller (2009), Evolution of the ice phase in tropical altocumulus: SAMUM lidar observations over Cape Verde, *J. Geophys. Res.*, *114*, D17208, doi:10.1029/2008JD011659.

Bower, K. N., S. J. Moss, D. W. Johnson, T. W. Choularton, J. Latham, P. R. A. Brown, A. M. Blyth, and J. Cardwell (1996), A parameterization of the ice water content observed in frontal and convective clouds, *Q. J. R. Meteorol. Soc.*, *122*, 1815–1844.

Carey, L. D., J. Niu, P. Yang, J. A. Kankiewicz, V. E. Larson, and T. H. Vonder Haar (2008), The vertical profile of liquid and ice water content in midlatitude mixed phase altocumulus clouds, *J. Appl. Meteorol. Clim.*, *47*, 2487–2495.

Cho, H. M., P. Yang, G. W. Kattawar, S. L. Nasiri, Y. Hu, P. Minnis, C. Trepte, and D. Winker (2008), Depolarization ratio and attenuated backscatter for nine cloud types: Analyses based on collocated CALIPSO lidar and MODIS measurements, *Opt. Express*, *16*, 3931–3948.

Clothiaux, E. E., T. P. Ackermann, G. G. Mace, K. P. Moran, R. T. Marchand, M. A. Miller, and B. E. Martner (2000), Objective determination of cloud heights and radar reflectivities using a combination of active remote sensors at the ARM CART sites, *J. Appl. Meteorol.*, *39*, 645–665.

Del Genio, A. D., M.-S. Yao, W. Kovari, and K. K.-W. Lo (1996), A prognostic cloud water parameterization for global climate models, *J. Clim.*, *9*, 270–304.

Deschamps, P. Y., F. M. Breon, M. Leroy, A. Podaire, A. Bricaud, J. C. Buriez, and G. Seze (1994), The POLDER mission: Instrument characteristics and scientific objectives, *IEEE Trans. Geosci. Remote Sens.*, *32*, 598–615.

Feigelson, E. M. (1978), Preliminary radiation model of a cloudy atmosphere. Part I- Structure of clouds and solar radiation, *Contrib. Atmos. Phys.*, *51*, 203–229.

Field, P. R., R. J. Hogan, P. R. A. Brownm A. J. Illingworth, T. W. Choularton, P. H. Kaye, E. Hirst and R. Greenaway (2004), Simultaneous radar and aircraft observations of mixed phase cloud at the 100 m scale, *Q. J. R. Meteorol. Soc.*, *130*, 1877–1904.

Fleishauer, R. P., V. E. Larson, and T. H. Vonder Haar (2002), Observed microphysical structure of midlevel, mixed phase clouds, *J. Atmos. Sci.*, *59*, 1779–1804.

Fridlind, A. M., A. S. Ackerman, G. McFarquhar, G. Zhang, M. R. Poellot, P. J. DeMott, A. J. Prenni, and A. J. Heymsfield (2007), Ice properties of single-layer stratocumulus during the Mixed-Phase Arctic Cloud Experiment (M-Pace): Part II. Model results, *J. Geophys. Res.*, *112*, D24202, doi:10.1029/2007JD008646.

Giraud, V., O. Thouron, J. Riedi, and P. Goloub (2001), Analysis of direct comparison of cloud top temperature and infrared split window signature against independent retrievals of cloud thermodynamic phase, *Geophys. Res. Lett.*, *28*(16), 983–986.

Goldsmith, J. E. M., F. H. Blair, S. E. Bisson, and D. D. Turner (1998), Turn-key Raman lidar for profiling atmospheric water vapor, clouds, and aerosols, *Appl. Opt.*, *37*, 4979–4990.

Gonzalez, R. C., and R. E. Woods (1992), *Digital Image Processing*, Addison-Wesley, 716 pp.

Haeffelin, M., et al. (2005), SIRTA, a ground-based atmospheric observatory for cloud and aerosol research, *Ann. Geophys.*, *23*, 253–275.
Heymsfield, A. J., L. M. Miloshevich, A. Slingo, K. Sassen, and D. O'C. Starr (1991), An observational and theoretical study of highly supercooled altocumulus, *J Atmos. Sci.*, *48*, 923–945.
Hogan, R. J., P. N. Francis, H. Flentje, A. J. Illingworth, M. Quante, and J. Pelon (2003a), Characteristics of mixed phase clouds: I. Lidar, radar and aircraft observations from CLARE'98, *Q. J. R. Meteorol. Soc.*, *129*: 2089–2116.
Hogan, R. J., A. J. Illingworth, E. J. O'Connor, and J. P. V. Poiares Baptista (2003b), Characteristics of mixed phase clouds: II. A climatology from ground-based lidar, *Q. J. R. Meteorol. Soc.*, *129*, 2117–2134.
Hogan, R. J., M. D. Behera, E. J. O'Connor, and A. J. Illingworth (2004), Estimate of the global distribution of stratiform supercooled liquid water clouds using the LITE lidar, *Geophys. Res. Lett.*, *31*, L05106, doi:10.1029/2003GL018977.
Hu, Y.-X., D. Winker, P. Yang, B. Baum, L. Poole, and L. Vann (2001), Identification of cloud phase from PICASSO-CENA lidar depolarization: a multiple scattering sensitivity study, *J. Quant. Spectrosc. Radiat. Transfer*, *70*, 569–579.
Intrieri, J. M., M. D. Shupe, T. Uttal, and B. J. McCarty (2002), An annual cycle of Arctic cloud characteristics observed by radar and lidar at SHEBA, *J. Geophys. Res.*, *107*(C10), 8030, doi:10.1029/2000JC000423.
Korolev, A. V., G. A. Isaac, S. G. Cober, J. W. Strapp, and J. Hallett (2003), Microphysical characterization of mixed phase clouds, *Q. J. R. Meteorol. Soc.*, *129*, 39–65.
Li, Z. X., and H. Le Treut (1992), Cloud-radiation feedbacks in a general circulation model and their dependence on cloud modeling assumptions, *Clim. Dyn.*, *7*, 133–139.
Lopez, P. (2002), Implementation and validation of a new prognostic large-scale cloud and precipitation scheme for climate and data-assimilation purposes, *Q. J. R. Meteorol. Soc.*, *128*, 229–257.
Matthais, V., and coauthors (2004), Aerosol lidar intercomparison in the framework of the EARLINET project: 1. Instruments, *Appl. Opt.*, *43*, 961–976.
McFarquhar, G. M., G. Zhang, M. R. Poellot, G. L. Kok, R. McCoy, T. Tooman, A. Fridlind, and A. J. Heymsfield (2007), Ice properties of single-layer stratocumulus during the mixed-phase arctic cloud experiment: 1. Observations, *J. Geophys. Res.*, *112*, D24201, doi:10.1029/2007JD008633.
Mitchell, J. F. B., C. A. Senior, and W. J. Ingram (1989), CO_2 and climate - A missing feedback, *Nature*, *341*, 132–134.
Moran, K. P., B. E. Martner, M. J. Post, R. A. Kropli, D. C. Welsh, and K. B. Widener (1998), An unattended cloud-profiling radar for use in climate research, *Bull. Am. Meteorol. Soc.*, *79*, 443–455.
Morille, Y., M. Haeffelin, P. Drobinski, and J. Pelon (2007), STRAT: An automated algorithm to retrieve the vertical structure of the atmosphere from single channel lidar data, *J. Atmos. Oceanic Technol.*, *24*, 761–775.
Morrison, H., and A. Gettelman (2008), A new two-moment bulk stratiform cloud microphysics scheme in the Community Atmosphere Model, version 3 (CAM3): Part I. Description and numerical tests, *J. Clim.*, *21*, 3642–3659.
Murayama, T., H. Okamoto, N. Kaneyasu, H. Kamataki, and K. Miura (1999), Application of lidar depolarization measurement in the atmospheric boundary layer: Effects of dust and sea-salt particles, *J. Geophys. Res.*, *104*(D24), 31,781–31,792.
Naud, C. M., A. Del Genio, and M. Bauer (2006), Observational constraints on cloud thermodynamic phase in midlatitude storms, *J. Clim.*, *19*, 5273–5288.
Newsom, R., D. D. Turner, B. Mielke, M. Clayton, and R. A. Ferrare (2009), The use of simultaneous analog and photon counting detection for Raman lidar, *Appl. Opt.*, *13*, 2712–2715.
Noel, V., and K. Sassen (2005), Study of planar ice crystal orientations in ice clouds from scanning polarization lidar observations, *J. Appl. Meteorol.*, *44*, 653–664.
Noel, V., H. Chepfer, G. Ledanois, and P. H. Flamant (2001), Computation of a single scattering matrix for nonspherical particles randomly or horizontally oriented in space, *Appl. Opt.*, *40*, 4365–4375.
Noel, V., H. Chepfer, G. Ledanois, A. Delaval, and P. H. Flamant (2002), Classification of particle shape ratios in cirrus clouds based on the lidar depolarization ratio, *Appl. Opt.*, *41*, 4245–4257.
Noel, V., M. Haeffelin, Y. Morille, and H. Chepfer (2006), Classification of ice crystal shapes in midlatitude ice clouds from three years of lidar observations over the SIRTA observatory, *J. Atmos. Sci.*, *63*, 2978–2991.
Platt, C. M. R. (1977), Lidar observations of a mixed phase altrostratus cloud, *J. Appl. Meteorol.*, *16*, 339–345.
Protat, A., A. Armstrong, M. Haeffelin, Y. Morille, J. Pelon, J. Delanoë, and D. Bouniol (2006), Impact of conditional sampling and instrumental limitations on the statistics of cloud properties derived from cloud radar and lidar at SIRTA, *Geophys. Res. Lett.*, *33*, L11805, doi:10.1029/2005GL025340.
Pruppacher, H. R., and J. D. Klett (1997), *Microphysics of Clouds and Precipitation*, 2nd ed. Kluwer Acad., Boston.
Rauber, R. M., and A. Tokay (1991), An explanation for the existence of supercooled water at the top of cold clouds, *J. Atmos. Sci.*, *48*, 1005–1023.
Riedi, J., P. Goloub, and R. T. Marchand (2001), Comparison of POLDER cloud phase retrievals to active remote sensors measurements at the ARM SGP site, *Geophys. Res. Lett.*, *28*(11), 2185–2188.
Rotstayn, L. D., N. F. Ryan, and J. J. Katzfey (2000), A scheme for calculation of the liquid cloud fraction in mixed phase stratiform clouds in large scale models, *Mon. Weather Rev.*, *128*, 1070–1088.
Sassen, K. (1980), Remote sensing of planar ice crystals fall attitude, *J. Meteorol. Soc. Jpn.*, *58*, 422–433.
Sassen, K. (1991), The polarization lidar technique for cloud research: A review and current assessment, *Bull. Am. Meteorol. Soc.*, *72*, 1848–1866.
Sassen, K., and P. L. Petrilla (1986), Lidar depolarization from multiple scattering in marine stratus clouds, *Appl. Opt.*, *25*, 1450–1459.
Sassen, K., and S. Benson (2001), A midlatitude cirrus cloud climatology from the Facility for Atmospheric Remote Sensing: Part II. Microphysical properties derived from lidar depolarization, *J. Atmos. Sci.*, *58*, 2103–2112.
Sassen, K., H. Zhao, and G. C. Dodd (1992), Simulated polarization diversity lidar returns from water and precipitating mixed phase clouds, *Appl. Opt.*, *31*, 2914–2923.
Shupe, M. D. (2007), A ground-based multisensor cloud phase classifier, *Geophys. Res. Lett.*, *34*, L22809, doi:10.1029/2007GL031008.
Shupe, M. D., S. Y Matrosov, and T. Uttal (2006), Arctic mixed phase cloud properties derived from surface-based sensors at SHEBA, *J. Atmos. Sci.*, *63*, 697–711.
Shupe, M. D., J. S. Daniel, G. de Boer, E. W. Eloranta, P. Kollias, C. N. Long, E. Luke, D. D. Turner, and J. Verlinde (2008), A focus on mixed phase clouds: The status of ground-based observational methods, *Bull. Am. Meteorol. Soc.*, *89*, 1549–1562. doi:10.1175/2008BAMS2378.1.
Turner, D. D., R. A. Ferrare, and L. A. Brasseur (2001), Average aerosol extinction and water vapor profiles over the Southern Great Plains, *Geophys. Res. Lett.*, *28*(23), 4441–4444.
Turner, D. D., R. A. Ferrare, L. A. Heilman Brasseur, W. F. Feltz, and T. P. Tooman (2002), Automated retrievals of water vapor and aerosol profiles from an operational Raman lidar, *J. Atmos. Oceanic Technol.*, *19*, 37–50.
Turner, D. D., S. A. Clough, J. C. Liljegren, E. E. Clothiaux, K. Cady-Pereira, and K. L. Gaustad (2007), Retrieving liquid water path and precipitable water vapor from Atmospheric Radiation Measurement (ARM) microwave radiometers, *IEEE Trans. Geosci. Remote Sens.*, *45*, 3680–3690.
Wang, Z., and K. Sassen (2001), Cloud type and macrophysical property retrieval using multiple remote sensors, *J. Appl. Meteorol.*, *40*, 1665–1682.
Wilson, D. R., and S. P. Ballard (1999), A microphysically based precipitation scheme for the UK Meteorological Office Unified Model, *Q. J. R. Meteorol. Soc.*, *125*: 1607–1636.
Winker, D. M., W. H. Hunt, and M. J. McGill (2007), Initial performance assessment of CALIOP, *Geophys. Res. Lett. 34*, L19803, doi:10.1029/2007GL030135.

J. Comstock and C. Lo, Pacific Northwest National Laboratory, P.O. Box 999, Richland, WA 99352, USA.
A. D. Del Genio and C. M. Naud, NASA Goddard Institute for Space Studies, 2880 Broadway, New York, NY 10025, USA. (cnaud@giss.nasa.gov)
J.-C. Dupont, M. Haeffelin, Y. Morille, and V. Noel, Laboratoire de Météorologie Dynamique and Institut Pierre Simon Laplace: Ecole Polytechnique, 91128 Palaiseau Cedex, France.
D. D. Turner, Space Science and Engineering Center, University of Wisconsin–Madison, 1225 West Dayton St., Madison, WI 53706, USA.